IEEE Transactions on Vehicular Technology

RIS-Assisted MIMO Channel Measurements and Characteristics Analysis for 6G Wireless Communication Systems

Journal:	*IEEE Transactions on Vehicular Technology*
Manuscript ID	VT-2023-04381.R1
Suggested Category:	Regular Paper
Date Submitted by the Author:	16-Mar-2024
Complete List of Authors:	Sun, Yingzhuo; Southeast University, ; Purple Mountain Laboratories, Wang, Cheng-Xiang; Southeast University, National Mobile Communications Research Laboratory; Purple Mountain Laboratories, Pervasive Communication Research Center Xu, Yingjie; Southeast University, ; Purple Mountain Laboratories, Xin, Lijian Huang, Jialing; Southeast University, National Mobile Communications Research Laboratory; Purple Mountain Laboratories, Huang, Jie; Southeast University, National Mobile Communications Research Laboratory, School of Information Science and Engineering, Southeast University qin, qibo Gao, Xinyu; Huawei Technologies Co Ltd, Guo, Bolun; Huawei Technologies Company Ltd., Research Department of Beijing R&D Subdivision, Wireless Network Cui, Tiejun ; Southeast University, State Key Laboratory of Millimeter Wave, School of Information Science and Engineering Chen, Yunfei; University of Durham, Department of Engineering; East China University of Science and Technology, School of Information Science and Engineering
Keywords:	6G wireless communication systems, channel measurements, channel characteristics, reconfigurable intelligent surface (RIS)

RIS-Assisted MIMO Channel Measurements and Characteristics Analysis for 6G Wireless Communication Systems

Yingzhuo Sun, Cheng-Xiang Wang, *Fellow, IEEE*, Yingjie Xu, Lijian Xin, *Member, IEEE*, Jialing Huang, Jie Huang, *Member, IEEE*, Qibo Qin, Xinyu Gao, Bolun Guo, Tie Jun Cui, *Fellow, IEEE*, and Yunfei Chen, *Senior Member, IEEE*

***Abstract*—Reconfigurable intelligent surface (RIS) can manipulate the electromagnetic (EM) waves in wireless channels and thus is promising for the sixth generation (6G) wireless communication systems. However, there exists little research on RIS channel measurements, which are important for the communication system design. In this paper, channel measurements are carried out in anechoic chamber, outdoor, and indoor environments. For anechoic chamber measurements, the insertion loss, EM response reciprocity, and received power are analyzed. It is found that RIS can fulfill EM response reciprocity. It is also found that the performance of RIS beamforming in the coplane configuration is better than that in the non-coplane configuration. In outdoor measurements, the cumulative distribution functions (CDFs) of large-scale parameters (LSPs) are obtained to explore the relationship between LSPs and heights. Results show that the RIS-user equipment (UE) channel is more sensitive to the height variation than the base station (BS)-RIS channel. For indoor measurements, the angular power spectral density (PSD), spatial cross-correlation function (CCF), and channel capacity are investigated. It is found that RIS with near-field coding and a larger size can bring a higher gain than RIS with far-field coding and a smaller size. The normalized power and code differences between near-field and far-field coding are defined to verify the RIS Rayleigh distance. It can be found that the value of the theoretical RIS Rayleigh distance is almost the same as the distance where the defined normalized differences become zero.**

***Index Terms*—6G wireless communication systems, channel measurements, channel characteristics, reconfigurable intelligent surface (RIS).**

This work was supported by the National Natural Science Foundation of China (NSFC) under Grants 61960206006 and 62271147, the Key Technologies R&D Program of Jiangsu (Prospective and Key Technologies for Industry) under Grants BE2022067 and BE2022067-1, the Fundamental Research Funds for the Central Universities under Grant 2242022k60006, the EU H2020 RISE TESTBED2 project under Grant 872172, the High Level Innovation and Entrepreneurial Doctor Introduction Program in Jiangsu under Grant JSSCBS20210082, the Start-up Research Fund of Southeast University under Grant RF1028623029, and the Fundamental Research Funds for the Central Universities under Grant 2242023K5003. *(Corresponding author: C.-X. Wang and J. Huang.)*

Y. Sun, C.-X. Wang, Y. Xu, J.-L. Huang, and J. Huang are with the National Mobile Communications Research Laboratory, School of Information Science and Engineering, Southeast University, Nanjing 210096, China, and also with the Purple Mountain Laboratories, Nanjing 211111, China (email: {yingzhuo_sun, chxwang, yjxu, jlhuang, j_huang}@seu.edu.cn).

L. Xin is with the Purple Mountain Laboratories, Nanjing 211111, China (email: xinlijian@pmlabs.com.cn).

Q. Qin is with Wireless Network RAN Research Department, Shanghai Huawei Technologies Co. Ltd., Shanghai 201206, China (e-mail: qinqibo1@huawei.com).

X. Gao and B. Guo are with the Research Department of Beijing R&D Subdivision, Wireless Network, Huawei Technologies Company Ltd., Beijing 100085, China (e-mail: {gaoxinyu,guobolun}@huawei.com).

T.-J. Cui is with the State Key Laboratory of Millimeter Wave, School of Information Science and Engineering, Southeast University, Nanjing 210096, China (email: tjcui@seu.edu.cn).

Y. Chen is with the Department of Engineering, University of Durham, Durham, U.K. OHI 3LE (email: Yunfei.Chen@durham.ac.uk).

I. Introduction

Reconfigurable intelligent surface (RIS), also known as intelligent reflecting surface (IRS) [1] or large intelligent surface (LIS) [2], is a type of artificial electromagnetic (EM) surface. RISs consist of periodically arranged EM units whose phase and amplitude responses can be manipulated to control incident EM waves in real time [3], [4]. Owing to the advantages such as easy to deploy, energy-efficient, and low-cost, it has been regarded as a promising key technology for the sixth generation (6G) wireless communications [5]–[7]. RIS has been applied in different ways and scenarios. In [8], it was used to provide extra spatial degrees of freedom through configuring the elements irregularly. In [9], it was employed in the optical wireless communication system. In the area of vehicular communications, RIS also plays an important role. In [10], it was used in the vehicular communication systems to implement the robust transmission with statistical channel state information. In [11], a method of RIS selection in vehicular communication network was introduced to realize a higher ergodic capacity. In [12], the authors jointly optimized the beamforming and the vehicle trajectory to minimize the power consumption. In [13], a joint optimization problem considering both the vehicle power allocation and RIS beamforming was discussed to maximize the throughput.

Channel modeling is important for the verification of key technologies and the evaluation of communication performances [14]–[19]. Meanwhile, wireless channel measurements aim to explore channel characteristics and thus help to construct the channel model more accurately. A large amount of experiments were conducted in anechoic chambers to explore the performance of manipulated RIS in different frequency bands or in different ways [20]–[22]. A comprehensive survey on the RIS experiments and channel measurements, channel characteristics analysis, as well as large-scale path loss models and small-scale multipath fading channel models was provided in [23]. Recently, more channel measurements have been conducted to further explore RIS channel characteristics. For example, in [24], channel measurements were conducted in the millimeter wave (mmWave) indoor scenario. Different multipath parameters were estimated and the angular power spectral density (PSD) was analyzed. In [25], the non-intelligent reflecting surfaces which were simply made of metal foils were employed in the THz indoor scenario. The measurement results showed that surfaces with larger sizes performed better than those with small sizes. The reflection losses and the coverage ratio were also calculated and analyzed. In [26], an efficient algorithm used to configure the RIS over the air was proposed. The indoor and outdoor tests were both conducted and the high power gain was observed in both two scenarios. In [27], a path loss model based on the radar cross section theory was proposed and validated. The distance between the transmitter and the receiver, the reflection angles, the effective area of RIS elements were considered in the proposed model. The measurement results validated the accuracy of the proposed model. In [28], a more effective path loss model was proposed and validated at the mmWave band. The properties of a single unit cell including scattering performance and power consumption were evaluated. The measurement results also confirmed that the model can characterize the power radiation of one unit cell. In [29], RIS was employed for measurements at 35 GHz to verify that RIS could combat multipath fading. A two-path propagation model was proposed, which considered both the direct path and the assisted path. Four types of RISs employing different configuration capabilities were introduced and compared through simulation results. In [30], the impact of RIS employed as the transmitter (Tx) in the indoor mmWave channel was investigated through experiments. The impacts of transmitting RIS on path loss, angular spreads (ASs), and delay spread (DS) were studied in particular. In [31], the authors proposed a RIS-assisted physical layer key generation algorithm in the multi-user communication system.

However, most existing channel measurements were conducted to study the performance of the RIS-assisted wireless communication systems or investigate the characteristics of the RIS-assisted channel in indoor and anechoic chamber scenarios. There are very few outdoor RIS channel measurements and even fewer segmented measurement experiments in outdoor environments. A RIS-assisted communication system is composed of the base station (BS), RIS, and user equipment (UE). This forms a BS-RIS-UE cascaded channel. It has two segments including BS-RIS sub-channel and RIS-UE sub-channel. It should be noticed that the words “Tx” and “the receiver (Rx)” here mean the channel measurement equipment which can transmit/receive the wireless signals with radio frequency (RF) chains. When conducting the segmented channel measurements for BS-RIS sub-channel, Tx is placed at the BS position and Rx is placed at the position of RIS to measure the channel between BS and RIS. When conducting the segmented channel measurements for RIS-UE sub-channel, Tx is set at the position of RIS and Rx is set at the position of UE to measure the channel between RIS and UE. Previous works only focused on the cascaded channel, not its segments. Moreover, limited small-scale fading analysis has been conducted in existing RIS channel measurements.

To fill the research gaps, the RIS-assisted single-input single-output (SISO) channel measurements in anechoic chambers, multiple-input multiple-output (MIMO) segmented channel measurements in outdoor environments, and MIMO cascaded channel measurements in indoor environments are carried out at 5.4 GHz. The employed RIS size has 24×24 elements. Far-field and near-field coding methods are designed for the experiments. Far-field coding only considers the phase differences caused by the projection differences of the incident wave on the array. Near-field coding considers the phase differences among RIS elements caused by the differences of the distance from each RIS element to Rx. The detailed calculation methods will be given later in section II. The main contributions and novelties of this paper are summarized as follows.

- Experiments in anechoic chambers are conducted to explore the EM characteristics of RIS. The EM response reciprocity of RIS is validated. The insertion losses under different coding modes are measured. The received power is compared in the coplane and the non-coplane conditions to validate the passive reflection characteristic of RIS.
- In outdoor scenarios, the BS-RIS channel measurements and RIS-UE channel measurements are conducted to explore channel characteristics on different RIS heights. Space alternating generalized expectation maximization (SAGE) algorithm is utilized to process the measurement data to obtain the multipath component parameters. Furthermore, the studied large-scale parameters (LSPs) of the two segmented channels include DS, ASs, and K-factor. Their cumulative distribution functions (CDFs) on different heights are presented and compared.
- RIS-assisted cascaded channel measurements are also conducted in indoor scenarios. Important characteristics including channel capacity and spatial cross-correlation function (CCF) are investigated and compared under different conditions.

The remainder of this paper is organized as follows. Section II describes channel measurement environments and measurement system setups. Section III presents the measurement data processing methods employing the high-resolution SAGE algorithm. Section IV presents the analysis results. Finally, conclusions are drawn in Section V.

II. RIS-assisted Channel Measurements

A. Measurement System Setups

The diagram of a time domain channel sounder is shown in Fig. 1. Tx is composed of a vector signal transceiver (VST) with a frequency range of 9 kHz–6 GHz band, a power amplifier (PA), a RF switch controller, a uniform planer array (UPA) or a horn antenna, and a global positioning system (GPS) Rubidium clock. Rx side includes an uniform cylindrical array (UCA), a RF switch controller, a low noise amplifier (LNA), a VST that can store the received signals, and a GPS Rubidium clock. A summary of the detailed equipment and parameters is given in Table I.

TABLE I
CHANNEL SOUNDER EQUIPMENT AND PARAMETERS.

Tx/Rx	Equipment	Parameters
Tx	VST	9 kHz–6 GHz band, 160 MHz bandwidth
	PA	500 MHz-6 GHz band, 35 dB gain
	Tx antenna	Anechoic chamber/Indoor measurements: Horn antenna Indoor/Outdoor measurements: Dual-polarized UPA with 32 elements
	Tx switch controller	32 channels in serial
Rx	VST	9 kHz–6 GHz band, 160 MHz bandwidth
	LNA	2 GHz-6 GHz band, noise floor 0.8 dB, 38 dB gain
	Rx antenna	Anechoic chamber/Indoor measurements: Horn antenna Indoor/Outdoor measurements: Dual-polarized UCA with 64 elements
	Rx switch controller	2 channels in parallel and 32 channels in serial

B. RIS Hardware and Coding Methods

There are four pieces of RIS hardware and they can be combined into different arrays with different sizes and shapes. One piece of RIS has 12×12 elements with a size of 0.312 m×0.312 m. It has a central frequency of 5.4 GHz with a bandwidth of 320 MHz. Each unit can be encoded with 4 different reflecting additive phases (0 coding: $0°$, 1 coding: $104.2°$, 2 coding: $181.7°$, and 3 coding: $284°$). There are two different coding modes, the far-field coding mode and the near-field coding mode. The continuous phase of each unit can be obtained under these two modes, which is calculated as [32]

$$\theta_{ij}^{\text{far}} = \mod\left(k(d_{ij}^{\text{T}} - d_0^{\text{T}} - \boldsymbol{v}_{ij} \cdot \boldsymbol{v}^{\text{R}}), 2\pi\right) \tag{1}$$

and

$$\theta_{ij}^{\text{near}} = \mod\left(k(d_{ij}^{\text{T}} - d_0^{\text{T}} - d_0^{\text{R}} + d_{ij}^{\text{R}}), 2\pi\right) \tag{2}$$

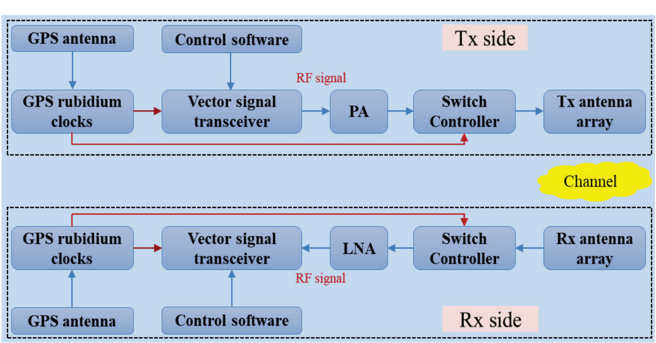

Fig. 1. The diagram of the measurement system setup.

TABLE II
MAPPING RELATIONSHIPS BETWEEN CONTINUOUS PHASES AND RIS CODES.

Continuous phases	Discrete phases	RIS codes
$(0°, 52.1°] \cup (322°, 360°]$	$0°$	0
$(52.1°, 142.95°]$	$104.2°$	1
$(142.95°, 232.85°]$	$181.7°$	2
$(232.85°, 322°]$	$284.0°$	3

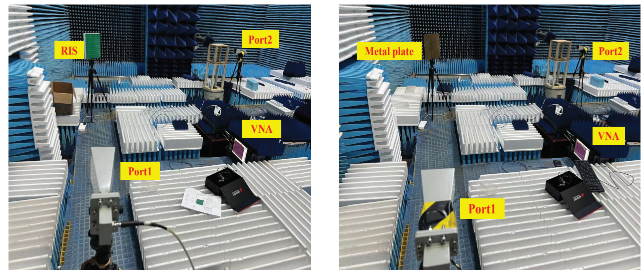

(a) (b)

Fig. 2. Insertion loss measurements of (a) RIS and (b) the metal plate.

where k denotes the wave number. The distances between Tx/Rx and each unit are denoted as d_{ij}^{T} and d_{ij}^{R}. The distances between the RIS center and Tx/Rx are denoted as d_0^{T} and d_0^{R}. The unit vector pointing from the RIS center to Rx is denoted as $\boldsymbol{v}^{\text{R}}$. The vector pointing from the RIS center to each unit is denoted as $\boldsymbol{v}_{ij}$. The discrete phase is the closest phase to the continuous one among the four phases corresponding four codes. The mapping relationship between the continuous angle values and the RIS codes is given in Table II. Another important property of the RIS hardware is that it can reverse the polarization direction of the impinging EM wave, meaning that a vertically/horizontally polarized EM wave will be converted into a horizontally/vertically polarized EM wave after being reflected by RIS.

C. RIS Measurements in Anechoic Chambers

In order to study the EM characteristics of the RIS, the measurement experiments are first carried out in an anechoic chamber. Note that only one piece of RIS is used in anechoic chamber measurements.

1) Insertion Loss Measurements: The insertion loss measurement scenario is shown in Fig. 2. Horn antennas are placed at the Tx side and the Rx side, connecting Port1 and Port2 of the vector network analyser (VNA), respectively. The coordinate values of the Tx antenna and the Rx antenna are $[0, 2.45, 0]$ and $[3.3, 0, 0]$, respectively. The EM responses S_{21} under different coding modes are recorded. Then, the RIS is replaced by a metal plate with the same size. The EM responses S_{21} in this case are also obtained. Therefore, the RIS insertion losses under different coding modes in the bandwidth are computed as the difference between S_{21} of RIS and that of the metal plate.

2) EM Response Reciprocity Measurements: The scenario for EM response reciprocity measurement is shown in Fig. 3. The center of RIS is defined as the axis origin, and Port1 of the VNA connects to a horn antenna with a location of

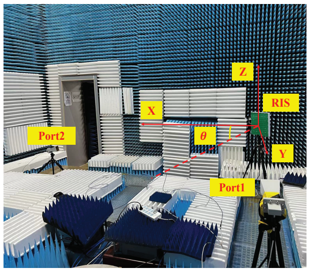

Fig. 3. EM response reciprocity measurement scenario of the RIS.

TABLE III
MEASUREMENT CASES FOR RECIPROCITY VERIFICATION.

Horn antenna positions on the Tx side and Rx side (m)		
Port1: [0,2.45,0]	Port2: [1.77,1,0]	$\theta = 90°$
	Port2: [1.6,0.58,0]	$\theta = 90°$
	Port2: [3.3,0,0]	$\theta = 60°$
	Port2: [1.6,0.58,0]	$\theta = 40°$
	Port2: [3.3,0,0.34]	$\theta = 45°$
	Port2: [3.3,0,-0.46]	$\theta = 45°$

$[0, 2.45, 0]$. The Port2 of the VNA is also connected to a horn antenna that is placed at different positions. Meanwhile, angles between the normal line of the RIS and the x-axis can also be changed through rotating RIS. A summary of the detailed measurement cases is shown in Table III. The code of the RIS is adjusted according to the position information of the horn antennas. The amplitudes and phases of S_{12} and S_{21} are recorded at the same time. The EM response reciprocity of the RIS is examined by comparing amplitudes and phases of S_{12} and S_{21}.

3) Received Power Measurements: The received power reflected by RIS from different directions is measured in an anechoic chamber equipped with a rotating platform and VNA. Two configurations are studied which are coplane and non-coplane configurations. The measurements of two configurations are given in Fig. 4, and the illustration of these two configurations is shown in Fig. 5. Tx and the normal line of RIS can constitute a plane which is denoted as $P_{Tx\text{-}Z}$. Rx and the normal line of RIS can constitute a plane which is denoted as $P_{Rx\text{-}Z}$. Coplane configuration means that $P_{Tx\text{-}Z}$ and $P_{Rx\text{-}Z}$ are the same plane. Non-oplane configuration means that $P_{Tx\text{-}Z}$ and $P_{Rx\text{-}Z}$ are different planes. The coordinate system based on the RIS center is also shown in Fig. 4. The Rx side position is fixed in two conditions. To shift the direction of the main lobe, codes are changed according to the expected direction. The angles of deviation from the normal line of RIS are 30°, 60°, and 90°. The measurement layout is shown in Table IV.

D. Outdoor RIS Segmented Channel Measurements

Segmented measurements of RIS-assisted channels in the outdoor environments are conducted. Because RIS tends to be deployed higher than UE but lower than BS to achieve better coverage [43], the path loss and LSPs of the BS-RIS channel and the RIS-UE channel are studied for different RIS heights. The outdoor measurement scenarios are shown in Fig. 6 (a).

1) BS-RIS Measurements: Tx is located at the position of BS at the B1 building with a height of 33 m, as shown in

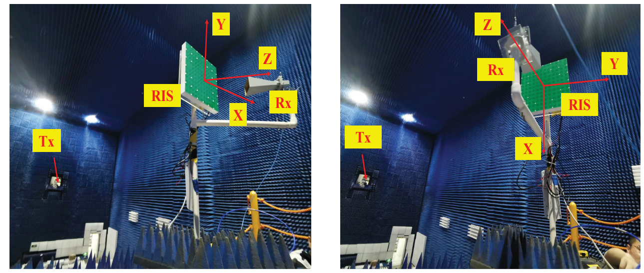

(a) (b)

Fig. 4. Received power measurements in an anechoic chamber under (a) the coplane configuration and (b) the non-coplane configuration.

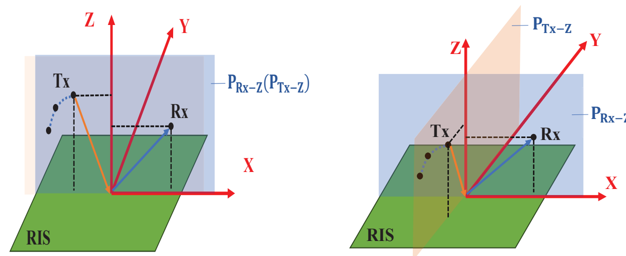

(a) (b)

Fig. 5. Illustration of received power measurements under (a) the coplane configuration and (b) the non-coplane configuration.

Fig. 6 (b). Rx antenna array equipped with 64 antenna elements is placed along Route 1 to receive the multipath signals. Note that Route 1 is evenly divided into 30 measurement positions marked as RIS1 to RIS30. The Rx antenna array is lifted from 3 m to 9 m with 1 m interval.

2) RIS-UE Measurements: In the RIS-UE sub-channel, Tx antenna array is located at RIS28 position on the heights of 3 m to 9 m above the ground. Rx antenna array is separately placed at Route 2 to receive the multipath signals, as shown in Fig. 6 (c). Route 2 is made of 30 evenly distributed measurement positions from UE1 to UE30.

E. Indoor RIS Cascaded Channel Measurements

RIS-assisted cascaded channel measurement scenarios are illustrated in Fig. 7. The detailed channel measurement parameters are shown in Table V. Scenarios of two sub-channels are shown in Fig. 8 (a) and Fig. 8 (b).

1) SISO Cascaded Channel Measurements: As illustrated in Table V, in Case1, RIS is placed in the propagation environment according to the diagram in Fig. 8 (c), where the angle between the normal line of RIS and the line connecting RIS center and Tx is 45°. The horn antenna on the Tx side transmits the EM signal sequences. The reflected EM signals are adjusted to the direction of Rx side by RIS. RIS is coded with far-field and near-field coding modes to compare the received power difference between two coding modes.

2) MIMO Cascaded Channel Measurements: To investigate more detailed channel characteristics, cascaded channel measurements under the condition of Tx/Rx equipped with multiple antennas are also carried out. The non-mirror reflection

TABLE IV
COORDINATE VALUES IN RECEIVED POWER MEASUREMENTS.

Condition	Rx position (m)	Tx position (m)
Coplane	[0.17,0,0.14]	[0,0,14]
		[-7,0,12.12]
		[-12.12,0,7]
Non-coplane	[0.08,0,0.28]	[0,0,14]
		[0,-7,12.12]
		[0,-12.12,7]

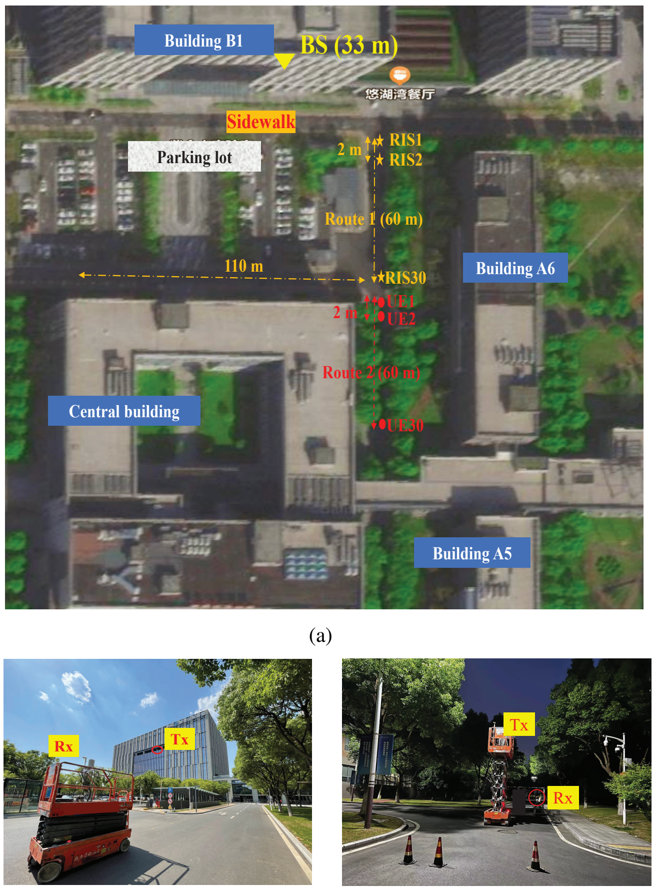

(a) (b) (c)

Fig. 6. The scenarios of (a) overall measurements, (b) BS-RIS channel measurements, and (c) RIS-UE channel measurements.

scenario is also introduced to be compared with the mirror reflection scenario. It is illustrated in Fig. 8 (d). The incident angle can be converted by means of rotating RIS. RISs with different sizes (24×24 elements and 12×36 elements) are also employed to investigate the influences of RIS's size.

III. MEASUREMENT DATA PROCESSING

A. Acquisition of CIR

To obtain the channel impulse response (CIR), measurement system calibration and data processing are needed to eliminate the effect of measurement equipment [33], [34]. The transmitted signal is denoted as $x(t)$. The response of the measurement system is defined as $g(t)$. The CIR is defined as $h(t)$. The received signal is $y(t)$. The Fourier transforms of $x(t)$, $g(t)$, $h(t)$, and $y(t)$ are denoted as $X(f)$, $G(f)$, $H(f)$, and $Y(f)$, respectively. $H(f)$ can be calculated as

$$H(f) = \frac{Y(f)}{X(f)G(f)}. \tag{3}$$

Then the CIR can be calculated as

$$h(t) = \text{IFFT}(H(f)) \tag{4}$$

where IFFT$(\cdot)$ is the inverse Fourier transform.

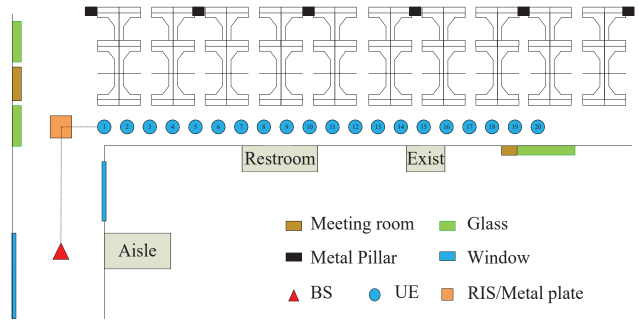

Fig. 7. The diagram of the measurement routes and positions in an indoor scenario.

TABLE V
INDOOR CASCADED CHANNEL MEASUREMENTS PARAMETERS.

Height	The same height for Tx, Rx, and the RIS center (1.7 m)
Case1	Mirror reflection, RIS with 24 × 24 elements
Case2	Non-RIS/non-metal plate
Case3	Mirror/non-mirror reflection, RIS with 24 × 24 elements
Case4	Mirror/non-mirror reflection, RIS with 24 × 24 elements
Case5	Mirror reflection, RIS with 12 × 36 elements

B. Channel Parameter Estimation

To extract the wireless multipath component (MPC) parameters, the high-resolution SAGE algorithm is implemented [35], [36]. Assume that there are M specular plane waves in the propagation environment, and that the numbers of the Rx antenna elements and Tx antenna elements are denoted as U and S. The received signal $\mathbf{Y}(t)$ can be written as

$$\mathbf{Y}(t) = \sum_{m=1}^{M} \mathbf{c}(\Omega_m^{\text{Rx}})\mathbf{A_m}\mathbf{c}(\Omega_m^{\text{Tx}})^T \exp(j2\pi\nu_m t)\mathbf{x}(t-\tau_m) + \sqrt{\frac{N_0}{2}}\mathbf{N}(t) \tag{5}$$

where $\mathbf{A}_m = \begin{bmatrix} \alpha_{m,1,1} & \alpha_{m,1,2} \\ \alpha_{m,2,1} & \alpha_{m,2,2} \end{bmatrix} = [\alpha_{m,p_1,p_2}]$ represents the polarization matrix and p_1, $p_2 \in [1,2]$ are chosen from two linear and orthogonal polarization orientations, ν_m denotes the Doppler frequency of the mth MPC, $\mathbf{\Omega}_m^{\text{Rx}}$ and $\mathbf{\Omega}_m^{\text{Tx}}$ are the angle of arrival and angle of departure of the mth MPC, respectively, τ_m is the delay of the mth MPC, $\mathbf{c}(\Omega_m^{\text{Rx}})$ and $\mathbf{c}(\Omega_m^{\text{Tx}})$ are antenna responses of the Rx and Tx antenna array, respectively, which can be measured in an anechoic chamber, $\mathbf{N}(t) \in \mathbb{C}^{U\times S}$ is the standard complex white Gaussian noise with PSD N_0. Therefore, the parameter set to be extracted for

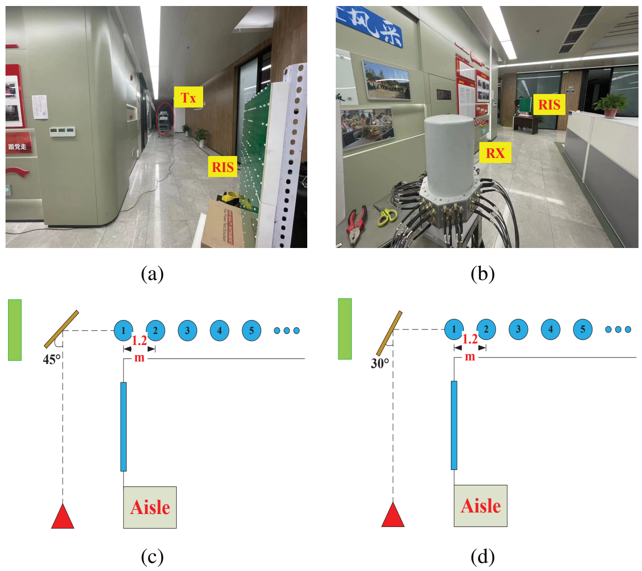

Fig. 8. The measurement scenarios of (a) the Tx-RIS link, (b) the RIS-Rx link, (c) mirror reflection measurement (45°), and (d) non-mirror reflection measurement (30°).

the mth MPC is $\mathbf{\Theta}_m = [\mathbf{A_m}, \mathbf{\Omega_m^{\mathrm{Rx}}}, \mathbf{\Omega_m^{\mathrm{Tx}}}, \tau_\mathbf{m}, \nu_\mathbf{m}]$, which can be estimated by using the SAGE algorithm in [34]. Note that $\mathbf{\Omega}_m^{\mathrm{Rx}}$ includes the azimuth angle of arrival (AoA) ϕ_m^{Rx} and the elevation angle of arrival (EoA) θ_m^{Rx} of the mth MPC, and $\mathbf{\Omega}_m^{\mathrm{Tx}}$ includes the azimuth angle of departure (AoD) ϕ_m^{Tx} and the elevation angle of departure (EoD) θ_m^{Tx} of the mth MPC.

C. Channel Characteristics

The root mean squared (RMS) DS is a second-order statistic, which is capable of describing the dispersion of the delay PSD. By using the estimated parameters, the DS can be formulated as

$$\tau_{rms} = \sqrt{\frac{\sum_{m=1}^{M} |\alpha_m|^2 \tau_m^2}{\sum_{m=1}^{M} |\alpha_m|^2} - \left(\frac{\sum_{m=1}^{M} |\alpha_m|^2 \tau_m}{\sum_{m=1}^{M} |\alpha_m|^2}\right)^2}. \quad (6)$$

The RMS AS can be used to illustrate the dispersion of the angular PSD. It is calculated by

$$\sigma_{rms} = \sqrt{\frac{\sum_{m=1}^{M} |\alpha_m|^2 \Omega_m^2}{\sum_{m=1}^{M} |\alpha_m|^2} - \left(\frac{\sum_{m=1}^{M} |\alpha_m|^2 \Omega_m}{\sum_{m=1}^{M} |\alpha_m|^2}\right)^2}. \quad (7)$$

Using (7), σ_{rms} can be obtained from the estimated angle $\Omega_m \in \{\phi_m^{\mathrm{Rx}}, \theta_m^{\mathrm{Rx}}, \phi_m^{\mathrm{Tx}}, \theta_m^{\mathrm{Tx}}\}$.

The spatial CCF is directly related to the channel characteristics [39]. The correlation coefficient between the CIR $\mathbf{h}_i$ of the ith Tx (Rx) antenna element and the CIR $\mathbf{h}_j$ of the jth Tx (Rx) antenna element is calculated by

$$\rho_{\mathbf{h}_i,\mathbf{h}_j} = \frac{\mathbf{E}\{(\mathbf{h}_i - \overline{h}_i)(\mathbf{h}_j - \overline{h}_j)\}}{\sqrt{\mathbf{E}\{(\mathbf{h}_i - \overline{h}_i)^2\}\mathbf{E}\{(\mathbf{h}_j - \overline{h}_j)^2\}}} \quad (8)$$

where $\mathbf{E}\{\cdot\}$ denotes the expectation operator. $\overline{h}_i$ and $\overline{h}_j$ denote the mean values of $\mathbf{h}_i$ and $\mathbf{h}_j$, respectively.

To study the relationship between the Rayleigh distance of RIS and received power difference under far-field and near-field coding modes, the normalized power difference and the normalized coding matrices difference are used. Note that this measurement is carried out employing horn antennas. The normalized difference of coding matrices at the nth measurement point is calculated as

$$c_n = \frac{\|\mathbf{C}_{n,\mathrm{far}} - \mathbf{C}_{n,\mathrm{near}}\|_F}{\max_n \|\mathbf{C}_{n,\mathrm{far}} - \mathbf{C}_{n,\mathrm{near}}\|_F} \quad (9)$$

where $\mathbf{C}_{n,\mathrm{far}}$ and $\mathbf{C}_{n,\mathrm{near}}$ are the coding matrices of the far-field coding mode and the near-field coding mode. Similarly, the normalized difference of power at the nth measurement point can be calculated as

$$p_n = \frac{|p_{n,\mathrm{far}} - p_{n,\mathrm{near}}|}{\max_n |p_{n,\mathrm{far}} - p_{n,\mathrm{near}}|} \quad (10)$$

where $p_{n,\mathrm{far}}$ and $p_{n,\mathrm{near}}$ denote the received power of the far-field coding mode and the near-field coding mode at the nth measurement point, respectively.

The end-to-end channel capacity is an important metric to evaluate the performance of the channel. This metric can reflect the general effects of channels, such as spatial CCF, Doppler spectrum, delay PSD, cross-polarization power ratio (XPR). The channel capacity of the measurement data can be expressed as [40]–[42]

$$C = \frac{1}{K} \sum_{k=1}^{K} \log_2 \det(\mathbf{I}_{M_\mathrm{R}} + \frac{\rho}{M_\mathrm{T}} \mathbf{H}(k)\mathbf{H}(k)^H) \quad (11)$$

where ρ is the signal-to-noise ratio (SNR), K denotes the number of frequency points, M_T and M_R are the numbers of Tx antennas and Rx antennas, respectively, $\mathbf{H}(k)$ is the channel transfer function matrix on the kth frequency point obtained after normalizing the original matrix by the factor of $\frac{1}{M_\mathrm{T} \cdot M_\mathrm{R} \cdot K}$, and $\mathbf{I}_{M_\mathrm{R}}$ is a unit matrix of order M_R.

IV. Channel Measurement Results and Analysis

In this section, channel measurement results are analyzed to explore the characteristics of RISs, RIS segmented channels, and RIS-assisted cascaded channels.

A. Anechoic Chamber RIS Measurements

To investigate the EM properties of the RIS, the measurements for the RIS composed of 12×12 units are carried out in an anechoic chamber, and the insertion loss of RISs and the EM reciprocity are studied as follows.

1) Insertion Loss: The insertion loss is shown in Fig. 9. In Fig. 9 (a), the values of S_{21} are shown. It can be observed that S_{21} of the metal plate is larger between 5.24 GHz and 5.56 GHz than S_{21} of RIS. Furthermore, S_{21} of RIS employing 2 and 3 coding patterns are more stable than those under 0 and 1 coding patterns.

When calculating the insertion loss, the S_{21} value of the metal plate is used as a benchmark. The insertion values of RIS

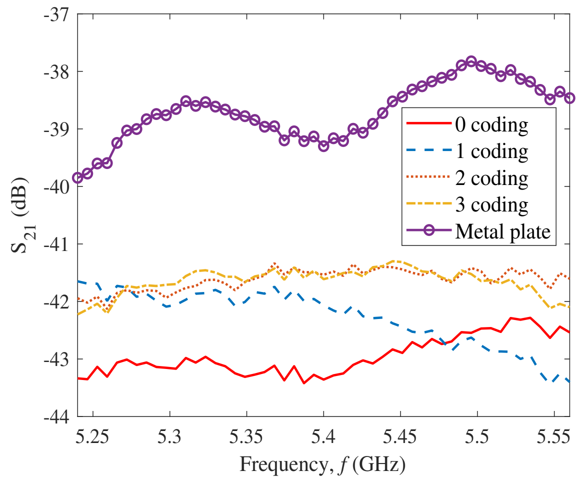

(a)

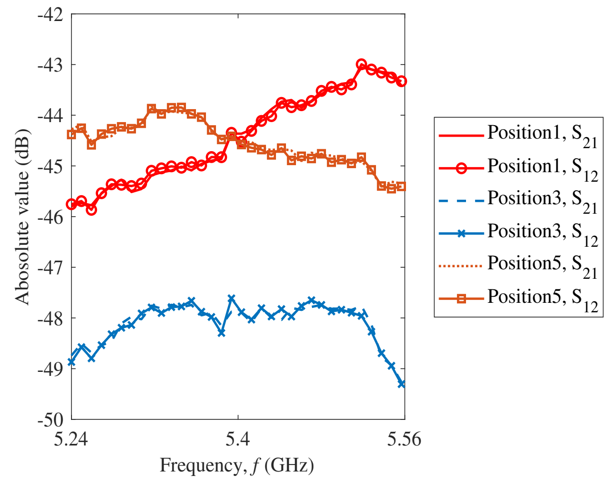

(a)

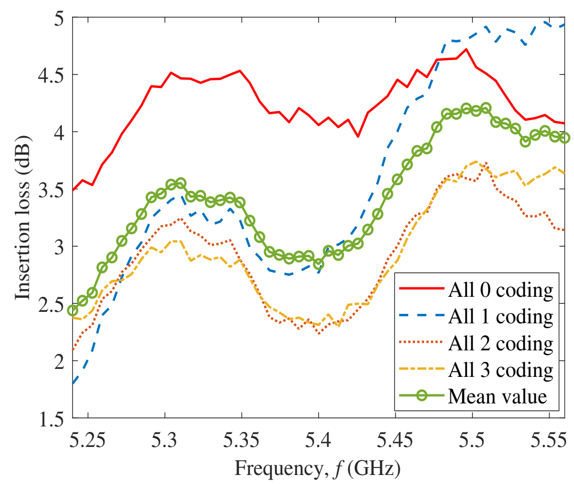

(b)

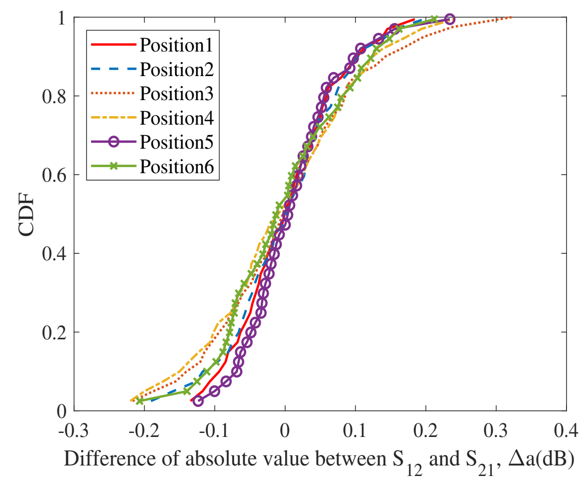

(b)

Fig. 9. Measurement results of (a) the S_{21} values and (b) the insertion losses of RIS.

Fig. 10. Absolute values of (a) S_{21} and S_{12} on different positions and (b) errors between S_{21} and S_{12}.

under different coding states are calculated as the differences between the S_{21} value of RIS and that of the metal plate. From Fig. 9 (b), the insertion loss under 0 coding fluctuates significantly within the measured bandwidth. The insertion losses under 2 and 3 coding are smaller than those under 0 and 1 coding states. The insertion loss of the RIS measured at 5.4 GHz is 2.84 dB by calculating the mean values of the insertion loss over all the coding states.

2) EM Response Reciprocity: In order to evaluate the EM response reciprocity, the magnitudes and the phases of both S_{21} and S_{12} are measured. Hence, EM response reciprocity of RIS can be validated by comparing S_{12} and S_{21}. Specifically, S_{21} matches with S_{12} very well, as shown in Fig. 10 (a). For simplicity, only three positions are studied in the figure. Furthermore, the error between S_{21} and S_{12} can be easily calculated. Then the CDFs of absolute errors on all measured frequency points for different positions are plotted in Fig. 10 (b). The value error is small within ± 0.2 dB. Similarly, the phase of S_{21} matches that of S_{12} very well as shown in Fig. 11 (a). At the same time, the error of the phase response between S_{21} and S_{12} is also small, which fluctuates within $\pm 2°$ as shown in Fig. 11 (b). It can be observed that the absolute values and the phases of S_{21} and S_{12} are almost the same, which confirms that RIS has the EM response reciprocity.

3) Received Power on Different Directions: In this measurement, the received power on different directions after adjusted by RIS is recorded, as depicted in Fig. 12. It can be observed that the received power of the coplane condition is much higher compared with that of the non-coplane condition. Furthermore, the difference between the power of the main lobe and that of side lobe under the coplane condition is higher than that of the non-coplane condition. Actually, the phenomenon mentioned above reflects the passively adjustable properties of RIS. It means that RIS can only control the reflecting direction of EM waves based on the rule of mirror reflection. In other words, the more the adjusted direction of the main lobe deviates from the mirror reflection direction, the less power is received. As a result, when Tx and Rx are not

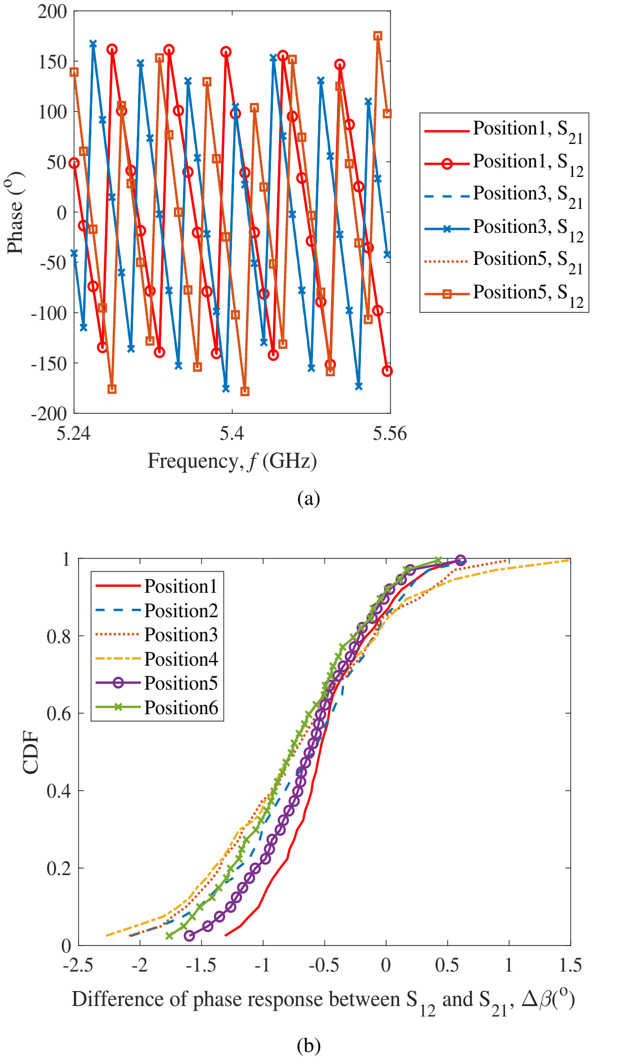

Fig. 11. Phases of (a) S_{21} and S_{12} on different positions and (b) errors between S_{21} and S_{12}.

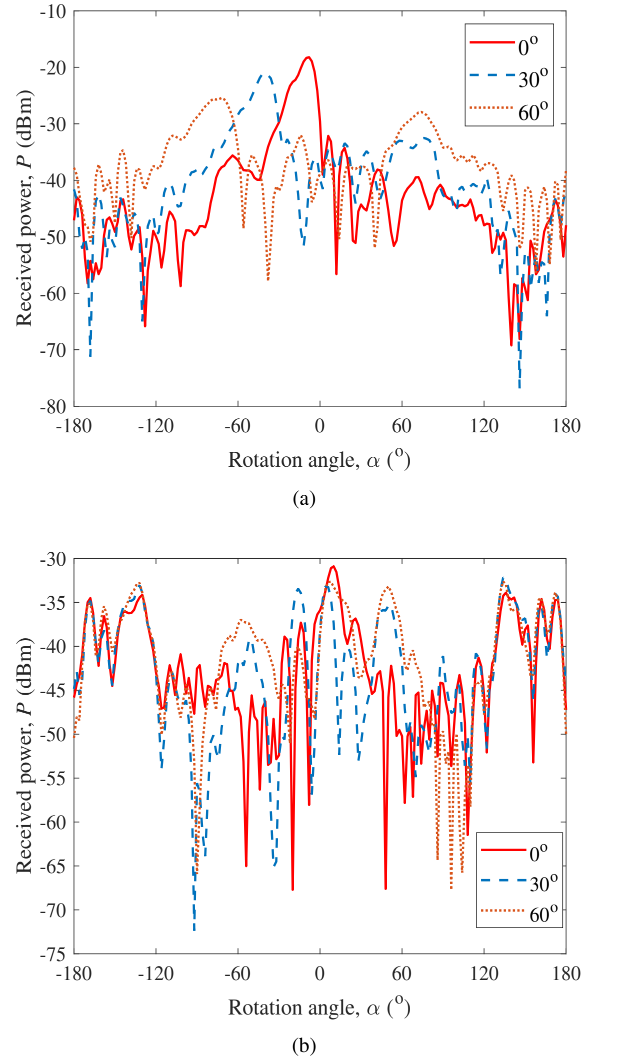

Fig. 12. Received power of (a) the coplane condition and (b) the non-coplane condition.

in the same plane with the normal line of RIS, the received power and the main lobe decrease dramatically.

B. Outdoor RIS Segmented Channel Measurement Results

Outdoor measurements of BS-RIS and RIS-UE sub-channels are carried out at 5.4 GHz. For each segmented channel, the delay PSD, and LSPs such as DS, azimuth angle spread of arrival (ASA), azimuth angle spread of departure (ASD), elevation angle spread of arrival (ESA), elevation angle spread of departure (ESD), and K-factor under different RIS heights are studied as follows.

1) Angular PSD: The angular PSDs of BS-RIS1 and RIS-UE1 on the height of 5 m are shown in Fig. 13. The angular PSD is calculated employing the bartlett estimation method. The accuracy of the measurement results can be guaranteed after comparing the measurement results with the real environment.

2) LSPs Analysis: The CDFs of LSPs of BS-RIS sub-channel at different Rx heights are given in Fig. 14, including DS, K-factor, ASA, ESA, ASD, and ESD. For clarity, the results of only three heights are shown in Fig. 14. The conclusions are drawn as follows. Firstly, due to the similar scatterer distribution at different Rx heights, there is little difference among the mean values of DS on different Rx heights, so are the variance values. Secondly, given that the propagation environment is more open as the Rx height increases, the proportion of the LOS components increases, which leads to the increase of the K-factor. Thirdly, the mean values of the ASA and ESA decrease when the Rx height increases. The main reason is that the number of scatterers around Rx antennas decreases with higher Rx heights, and the reflection path from the ground will become weaker, resulting in a smaller extension of the angle of arrival. Moreover, due to the similar scatterer distributions at different measurement points on the same Rx height, the variances of the ASA and ESA are all small on different heights. The variance of ASA varies form 1.55 to 1.9 and that of ESA varies from 1.25 to 1.6, respectively. Fourthly, the mean values and variance values of

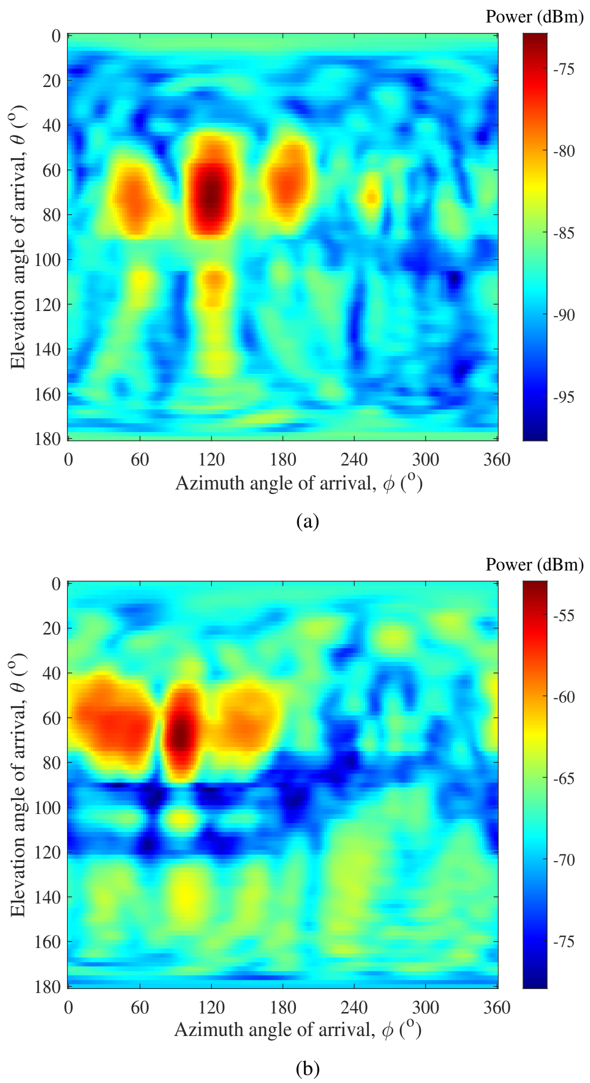

Fig. 13. The measured angular PSDs of (a) BS-RIS1 channel at the height of 5 m and (b) RIS-UE1 channel at the height of 5 m.

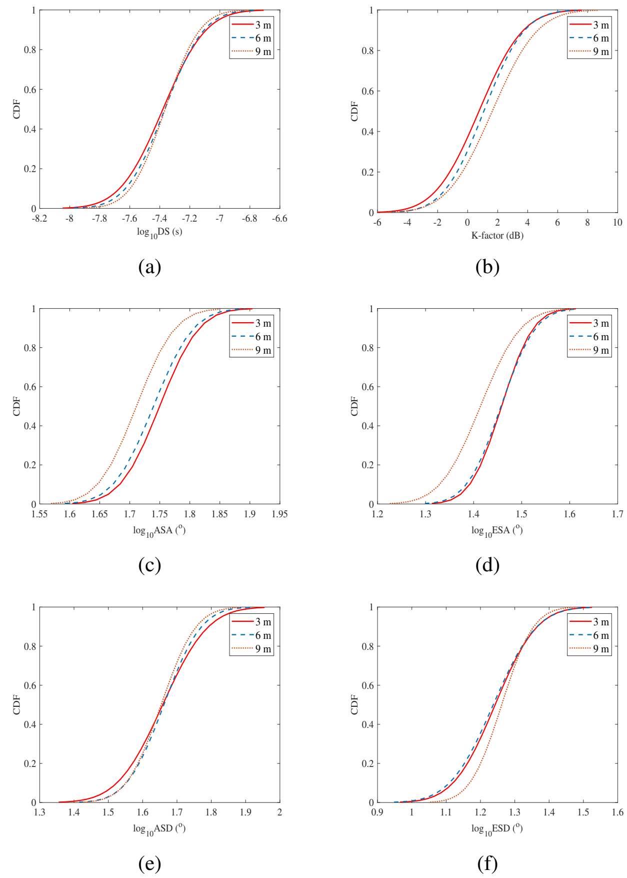

Fig. 14. CDFs of the LSPs for the BS-RIS sub-channel: (a) DS, (b) K-factor, (c) ASA, (d) ESA, (e) ASD, and (f) ESD.

both the ASD and ESD almost remain unchanged at different Rx heights. The reason for this is that the distance between Tx and Rx is far and the scattering environment on the Tx side hardly changes even if Rx antennas rise.

Similarly, CDFs of the LSPs of the RIS-UE sub-channel at different Rx heights are also shown in Fig. 15. For clarity, the results of only three heights are shown in Fig. 15. Firstly, because the scatterer distribution changes little at different Rx heights, the mean values of DS are close to each other. Moreover, the variance of DS becomes smaller with the increase of the Rx height. The reason is that scatterer distributions from the DS perspective on the same height change little among different measurement points. Secondly, the K-factor increases with the increase of the Rx height. The reason is that the ratio of the LOS path becomes higher with the increase of the RIS height. Thirdly, the mean and variance of the ASA and ASD are almost unchanged when the Rx height increases, as the horizontal position between Rx and Tx is unchanged, and the LOS path is the main component. Therefore, the scatterers at Rx and Tx side in the azimuth angle will not change with the increase of height or the change of the Rx point. Fourthly, the mean values and the variance values of both ESA and ESD increase with the increase of the Rx height. The reason is that the ground reflection path increases with the increase of the Rx height, leading to the increase of the elevation ASs.

In Fig. 16, the correlation coefficients of different LSPs of BS-RIS and RIS-UE sub-channels over the height difference are shown. It can be found that the autocorrelation function of RIS-UE decreases faster than that of BS-RIS sub-channel. This is mainly because the height of Tx in BS-RIS sub-channel is much higher than the variation of Rx height. However, the difference between Tx height and Rx height of RIS-UE sub-channel is smaller. As a result, RIS-UE sub-channel is more sensitive to the variation of the Tx height.

C. *Indoor RIS Cascaded Channel Measurement Results*

The power of Rx antennas, angular PSD, spatial CCF, and channel capacity are studied as follows.

1) Received Power: All 16 vertically polarized Tx antennas are used to transmit the EM signals. Since the RIS can cause polarization reversals of waves, 24 horizontally polarized Rx antennas are employed to receive EM waves coming from RIS. At the same time, because metal plates cannot change the polarization of EM wave, 24 vertically polarized antennas which

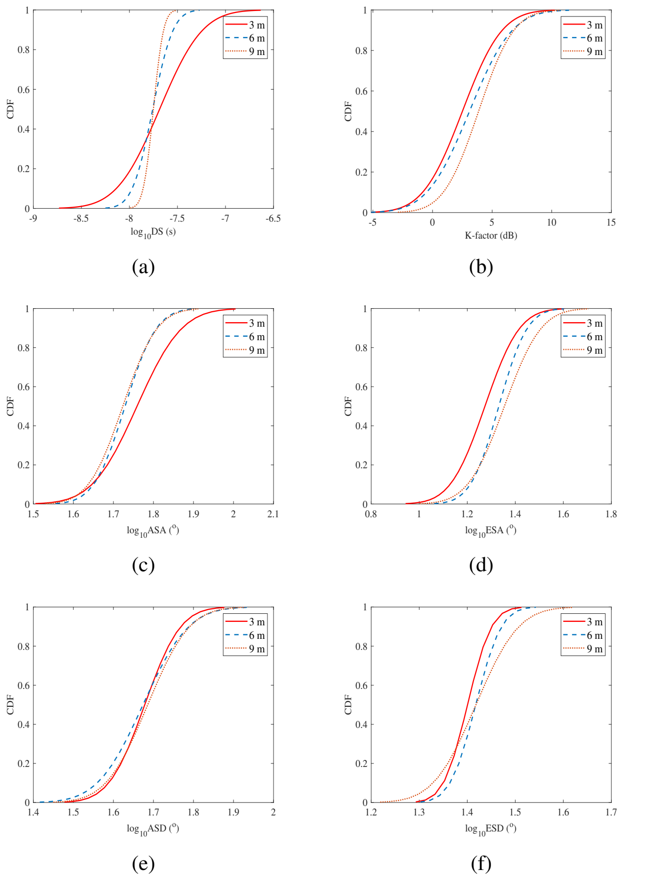

Fig. 15. CDFs of the LSPs for the RIS-UE sub-channel: (a) DS, (b) K-factor, (c) ASA, (d) ESA, (e) ASD, and (f) ESD.

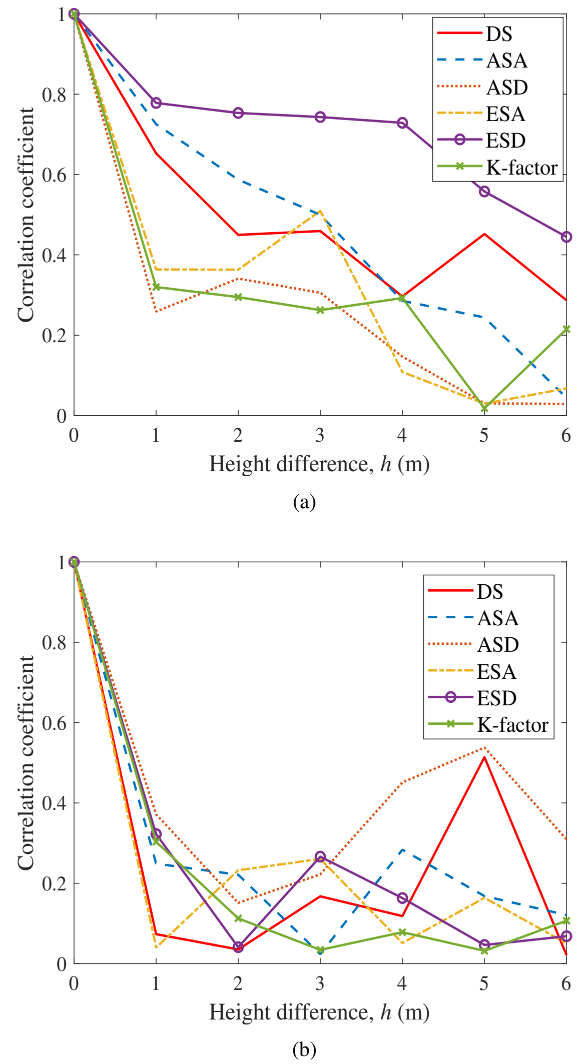

Fig. 16. The autocorrelation function over the vertical direction for (a) the BS-RIS sub-channel and (b) the RIS-UE sub-channel.

have the same location as the 24 horizontally just mentioned on the UCA are employed at Rx side. When conducting the cascaded channel measurement, the metal plate and the RIS are individually placed at the same reflection position. The RIS has the same size as the metal plate. The average power of each Rx antenna is shown in Fig. 17 (a) under the mirror reflection scenario. Obviously, the average received power of the non-RIS/non-metal plate-assisted channel is the lowest, but the average received power of the metal plate-assisted channel is larger than that of channel assisted by RIS with 24×24 elements. The average power of three channel measurements is -83.22 dBm, -80.48 dBm, and -83.19 dBm. The reason is that the whole metal plate is a conductor and can approximately reflect EM signals towards the Rx antennas under the mirror reflection condition, but the effective area of the RIS is much smaller than that of the metal plate even if the RIS can generate a narrow beam towards Rx antennas. Except for the direct signal, more scattering signals can be received by the antennas after being reflected by the wall. Therefore, the reflection gain of the metal plate is greater than the regulation gain of the RIS. Hence, the received power increases after being reflected by the metal plate.

The average power of each Rx antenna is further studied in Fig. 17 (b) under the non-mirror reflection scenario. The average power of the non-RIS/non-metal plate-assisted channel, metal plate-assisted channel, and RIS-assisted channel is -83.23 dBm, -82.67 dBm, and -82.31 dBm, respectively. Compared with the channel measurements under the mirror reflection scenario, the function of the metal plate is limited, and the beamforming of the RIS is more significant.

It can be observed in Fig. 18 that normalized differences of power and code matrix decrease with the measurement points extending in a similar trend. They both fall to almost zero at about the distance of 25 m. Meanwhile, the Rayleigh distance of RIS with 24×24 elements is calculated as $L = \frac{2D^2}{\lambda}$ where L is the Rayleigh distance, D is the length of the diagonal line, and λ is the wavelength. So the Rayleigh distance of the measured RIS is 28 m. As a result, it can be deduced that measuring the differences of power or code matrices between two coding modes can be a good method of estimating the Rayleigh distance.

2) Angular PSD: The angular PSDs of the non-RIS/non-metal plate-assisted channel, metal plate-assisted channel, and RIS-assisted channel are further explored. Specifically, the

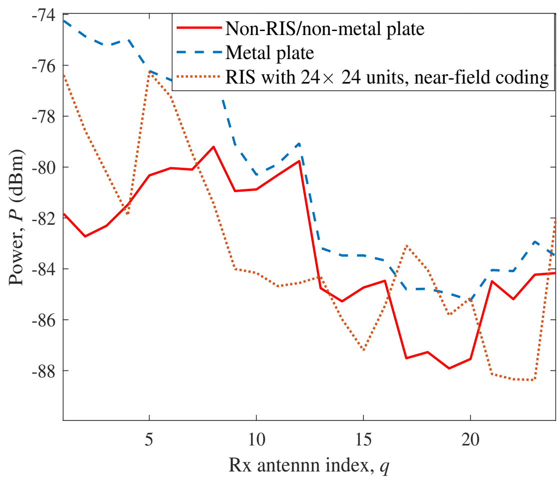

(a)

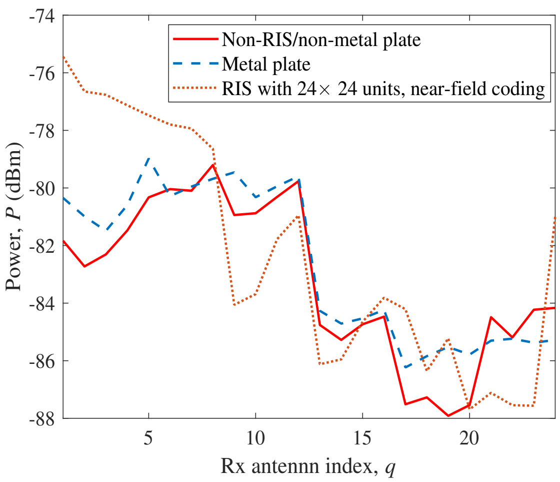

(b)

Fig. 17. Power of Rx antenna indexes for (a) the mirror reflection scenario and (b) the non-mirror reflection scenario.

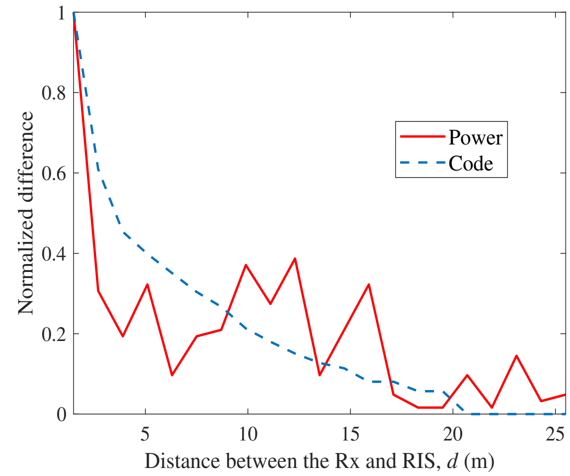

Fig. 18. Power and code differences with variation of the distance between the Rx and RIS.

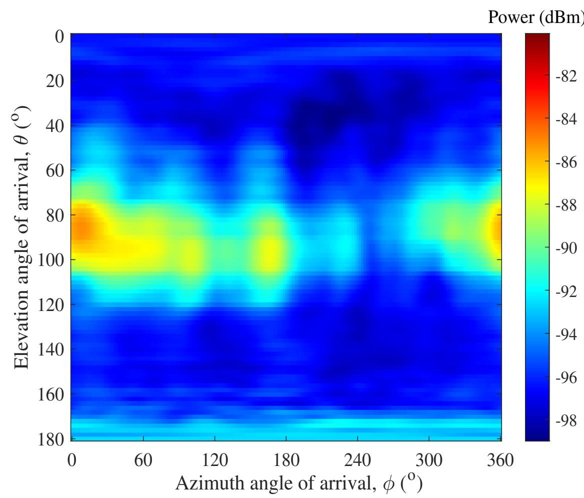

Fig. 19. Angular PSD of the non-RIS/non-metal plate-assisted channel measurements in an indoor scenario.

angular PSD of the non-RIS/non-metal plate-assisted channel observed at Rx5 is given in Fig. 19. Multipaths can be observed due to the reflectors in the office. Furthermore, the angular PSDs of the metal plate-assisted channel and RIS-assisted channel are shown in Fig. 20 (a) and Fig. 20 (b) in the mirror reflection scenario. We can observe a target wave of around $(90°, 90°)$ even if the beamforming power of the metal plate-assisted channel is lower than that of the RIS-assisted channel. However, the side lobe of beam for metal plate-assisted channel is larger than that of the RIS-assisted channel. The results also confirm that more scattering signals can be received by the antennas after being reflected by the wall in the metal plate-assisted channel measurement. Channel measurements under the non-mirror reflection scenario are carried out for the metal plate-assisted channel and the RIS-assisted channel. Measurement results are given in Fig. 20 (c) and Fig. 20 (d). The metal plate and RIS can bring new MPCs, but the directions and strengths of the MPCs are different. In the non-mirror reflection condition, most of the signals reflected by the metal plate cannot be received by Rx antennas, but RIS can intelligently adjust waves to Rx. Specifically, the RIS can bring a gain of about 7 dB while the metal plate can bring a gain of about 3 dB. Thus, the RIS is superior to the metal plate under the non-mirror reflection condition.

3) Spatial CCF: In Fig. 21, the spatial CCF based on 4 vertically polarized Tx antennas which are distributed on one column of the 4×4 Tx antenna array and one horizontally antenna element at Rx side is calculated. In the mirror reflection condition, the spatial CCF of the Tx antennas of the RIS-assisted channel is similar to that of the metal-assisted channel. This also confirms that the metal plate can play the role of the RIS in mirror reflection scenarios. Due to the existing multiple reflectors in the office environment, the MPCs coming from different directions are received by the Rx antenna array. Therefore, the spatial CCF between Tx antennas for the non-RIS/non-metal plate-assisted channel is smaller than that under the metal plate-assisted channel and RIS-assisted channel, as illustrated in Fig. 21 (a). In Fig. 21 (b),

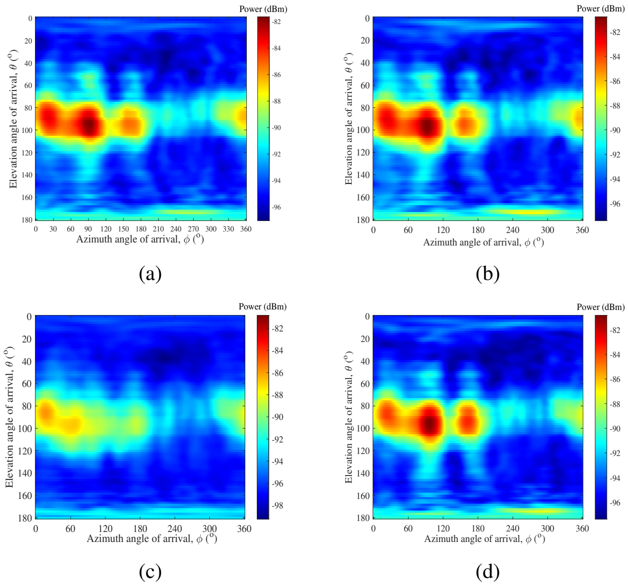

Fig. 20. Angular PSDs of indoor channel measurements in (a) the metal plate-assisted mirror reflection scenario, (b) the RIS-assisted mirror reflection scenario, (c) the metal plate-assisted non-mirror reflection scenario, and (d) the RIS-assisted non-mirror reflection scenario.

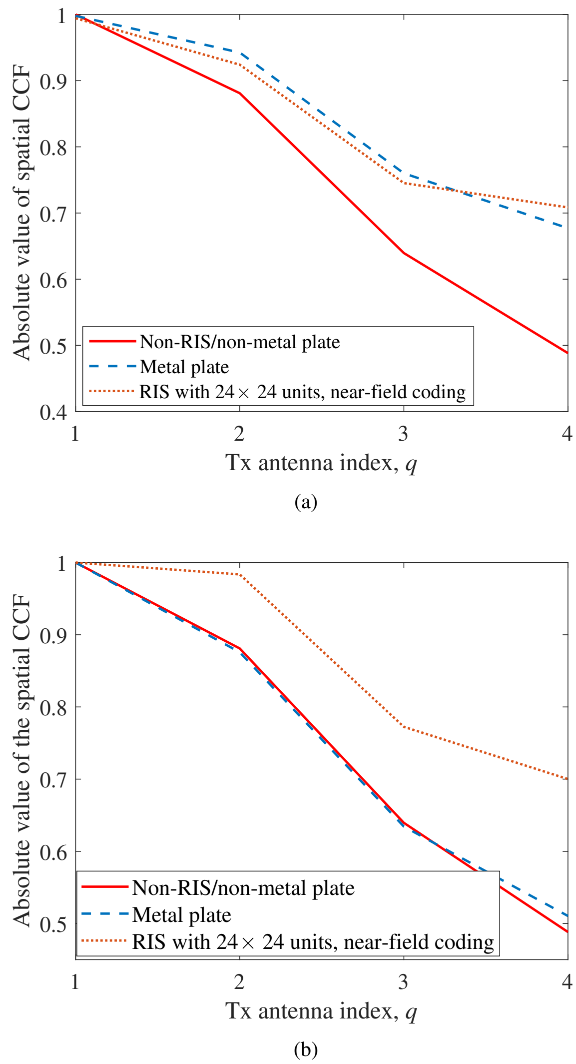

Fig. 21. Spatial CCFs in (a) mirror reflection scenarios and (b) non-mirror reflection scenarios.

the spatial CCF of the metal plate-assisted channel is lower than that of the channel assisted by RIS with 24×24 elements under the near-field coding, but close to that of the non-RIS/non-metal plate-assisted channel when it is in the non-mirror reflection scenario.

One important issue to be studied in the cascaded channel measurements is the impacts of the RIS size and coding modes on the RIS-assisted channel, which is given in Fig. 22. First, since RIS with 24×24 elements is composed of more units than the RIS with 12×36 elements, the beam is narrower. Therefore, the spatial CCF for the channel assisted by RIS with 24×24 elements is larger than that of the channel assisted by RIS with 12×36 elements. Second, since all Rx positions are located in the near-field of RIS EM radiation, the beam formed by the RIS under the near-field coding mode is narrower than that formed under the far-field coding mode. Therefore, the spatial CCF of the RIS-assisted channel using near-field coding is higher than that of the RIS-assisted channel using far-field coding.

4) Channel Capacity: In Fig. 23, when the reflecting object is placed at the non-mirror reflection situation, the channel capacity of the metal plate-assisted channel is lower than that of the 24×24-unit RIS-assisted channel using the near-field coding and close to that of the non-RIS/non-metal plate-assisted channel, which is consistent with the received power and the angular PSD results. Note that the channel capacity is very small for different cascaded channels, as the path loss is taken into account in the CIR when calculating channel capacity based on (11).

Furthermore, Fig. 24 shows the impacts of the RIS size and coding mode on the channel capacity of the RIS-assisted channel. Thus, a larger RIS brings a higher gain for Rx antennas, so the channel capacity is larger. Also, the beam gain formed by the RIS using the near-field coding mode is larger than that formed by the far-field coding mode. Hence, the channel capacity of the RIS-assisted channel using the near-field coding is larger.

V. Conclusions

In this paper, we have conducted various RIS-assisted channel measurements, including the EM response measurements in the anechoic chamber, the segmented MIMO channel measurements in outdoor environments, and the cascaded channel measurements in an indoor environment. The SAGE algorithm has been used to extract the MPC information in indoor and outdoor measurements.

In anechoic chamber measurements, it has been found that the insertion loss of the measured RIS is around 2.84 dB, and that RIS satisfies the EM response reciprocity. It has been found that the performance of RIS under the coplane condition is better than that under the non-coplane condition. In outdoor

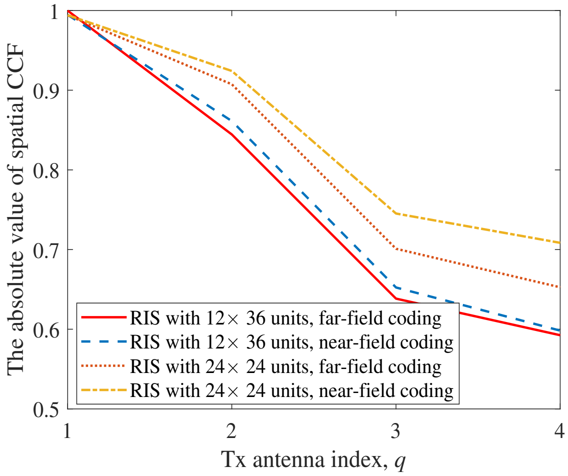

Fig. 22. Spatial CCFs of the channel measurements under different RIS sizes and coding methods.

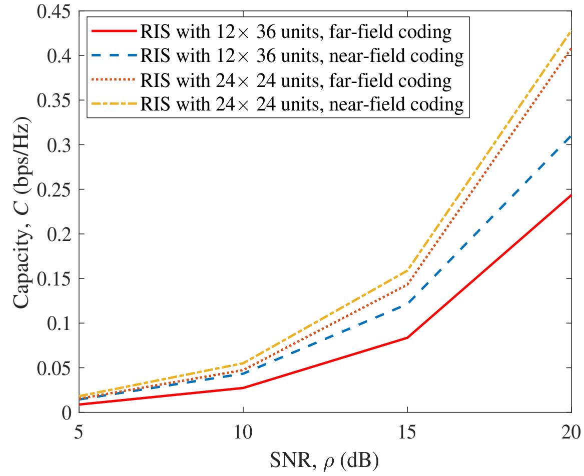

Fig. 24. Channel capacities of the channel measurements under different RIS sizes and coding methods.

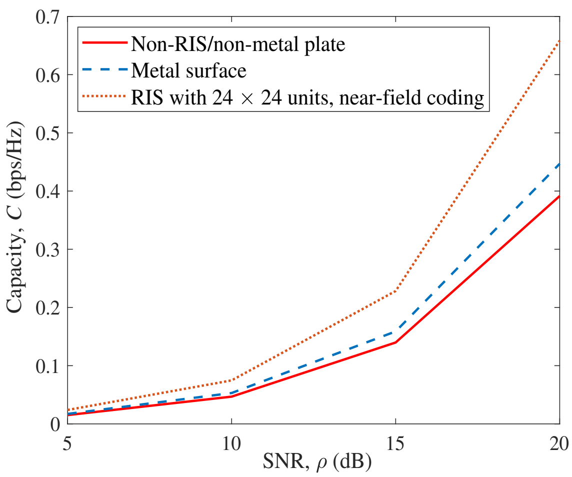

Fig. 23. Channel capacities of indoor channel measurements in non-mirror reflection scenarios.

channel measurements, CDFs of six LSPs in BS-RIS sub-channel and RIS-UE sub-channel on different heights have been compared, and the phenomenon have been explained. Moreover, the correlation function of BS-RIS sub-channel decreases more slowly than that of RIS-UE sub-channel. In indoor channel measurements, it has been found that the coding modes and RIS sizes can change the channel properties. Compared with the metal plate, the RIS with the same size can effectively improve the power of the target signal and increase the channel capacity for the non-mirror reflection scenarios. It has been found that measuring the differences of power or code could be a good method of estimating the Rayleigh distance of RIS.

REFERENCES

[1] Q. Wu and R. Zhang, "Towards smart and reconfigurable environment: Intelligent reflecting surface aided wireless network," *IEEE Commun. Mag.*, vol. 58, no. 1, pp. 106–112, Jan. 2020.

[2] Y.-C. Liang, R. Long, Q. Zhang, J. Chen, H. V. Cheng, and H. Guo, "Large intelligent surface/antennas (LISA): Making reflective radios smart," *J. Commun. Inf. Netw.*, vol. 4, no. 2, pp. 40–50, June 2019.

[3] Y. Liu, X. Liu, X. Mu, *et al.*, "Reconfigurable intelligent surfaces: Principles and opportunities," *IEEE Commun. Surveys Tuts.*, vol. 23, no. 3, pp. 1546–1577, May 2021.

[4] W. Tang, M. Chen, J. Dai, *et al.*, "Wireless communications with programmable metasurface: New paradigms, opportunities, and challenges on transceiver design," *IEEE Wireless Commun.*, vol. 27, no. 2, pp. 180–187, Jan. 2020.

[5] C.-X. Wang, X. You, X. Q. Gao, *et al.*, "On the road to 6G: Visions, requirements, key technologies and testbeds," *IEEE Commun. Surveys Tuts.*, vol. 25, no. 2, pp. 905–974, Secondquarter, 2023, doi: 10.1109/COMST.2023.3249835.

[6] X.-H. You, C.-X. Wang, J. Huang, *et al.*, "Towards 6G wireless communication networks: Vision, enabling technologies, and new paradigm shifts," *Sci. China Inf. Sci.*, vol. 64, no. 1, Jan. 2021.

[7] A. L. Moustakas, G. C. Alexandropoulos, and M. Debbah, "Reconfigurable Intelligent Surfaces and Capacity Optimization: A Large System Analysis," *IEEE Trans. Wireless Commun.*, vol. 22, no. 12, pp. 8736-8750, Dec. 2023.

[8] R. Su, L. Dai, J. Tan, M. Hao, and R. MacKenzie, "Capacity enhancement for reconfigurable intelligent surface-aided wireless network: from regular array to irregular array," *IEEE Trans. Veh. Technol.*, vol. 72, no. 5, pp. 6392-6403, May 2023.

[9] H. Wang, Z. Zhang, B. Zhu, *et al.*, "Performance analysis of multi-branch reconfigurable intelligent surfaces-assisted optical wireless communication system in environment with obstacles," *IEEE Trans. Veh. Technol.*, vol. 70, no. 10, pp. 9986-10001, Oct. 2021.

[10] Y. Chen, Y. Wang, and L. Jiao, "Robust transmission for reconfigurable intelligent surface aided millimeter wave vehicular communications with statistical CSI," *IEEE Trans. Wireless Commun.*, vol. 21, no. 2, pp. 928-944, Feb. 2022.

[11] N. Mensi, and D. B. Rawat, "Reconfigurable intelligent surface selection for wireless vehicular communications," *IEEE Wireless Commun. Lett.*, vol. 11, no. 8, pp. 1743-1747, Aug. 2022.

[12] A. B. M. Adam, X. Wan, M. A. M. Elhassan, *et al.*, "Intelligent and robust UAV-aided multiuser RIS communication technique with jittering UAV and imperfect hardware constraints," *IEEE Trans. Veh. Technol.*, vol. 72, no. 8, pp. 10737-10753, Aug. 2023.

[13] Y. Yu, X. Liu, Z. Liu, and T. S. Durrani, "Joint trajectory and resource optimization for RIS assisted UAV cognitive radio," *IEEE Trans. Veh. Technol.*, vol. 72, no. 10, pp. 13643-13648, Oct. 2023.

[14] J. Bian, C.-X. Wang, X. Gao, X.-H. You, and M. Zhang, "A general 3D non-stationary wireless channel model for 5G and beyond," *IEEE Trans. Wireless Commun.*, vol. 20, no. 5, pp. 3211–3224, May 2021. doi: 10.1109/TWC.2020.3047973

[15] C.-X. Wang, Z. Lv, X. Gao, X.-H You, Y. Hao, and H. Haas, "Pervasive wireless channel modeling theory and applications to 6G GBSMs for all

frequency bands and all scenarios," *IEEE Trans. Veh. Technol.*, vol. 71, no. 9, pp. 9159–9173, Sept. 2022.

[16] C.-X. Wang, J. Huang, H. Wang, X. Gao, X.-H You, and Y. Hao, "6G wireless channel measurements and models: Trends and challenges," *IEEE Veh. Technol. Mag.*, vol. 15, no. 4, pp. 22–32, Dec. 2020.

[17] G. Sun, R. He, B. Ai, *et al.,* "A 3D wideband channel model for RIS-assisted MIMO communications," *IEEE Trans. Veh. Technol.*, vol. 71, no. 8, pp. 8016-8029, Aug. 2022.

[18] Z. Lian, Y. Su, Y. Wang, and L. Jiang, "A non-stationary 3-D wideband channel model for intelligent reflecting surface-Assisted HAP-MIMO communication systems," *IEEE Trans. Veh. Technol.*, vol. 71, no. 2, pp. 1109-1123, Feb. 2022.

[19] Y. Ni, Y. Liu, J. Wang, Q. Wang, H. Zhao, and H. Zhu, "Performance analysis for RIS-assisted D2D communication under Nakagami-m fading," *IEEE Trans. Veh. Technol.*, vol. 70, no. 6, pp. 5865-5879, June 2021.

[20] L. Li, T.-J. Cui, W. Ji, *et al*. "Electromagnetic reprogrammable coding-metasurface holograms," *Nat Commun* 8, 197 (2017). https://doi.org/10.1038/s41467-017-00164-9

[21] S. Liu, T.-J. Cui, Q. Xu, *et al*. "Anisotropic coding metamaterials and their powerful manipulation of differently polarized terahertz waves," *Light Sci Appl* 5, e16076 (2016). https://doi.org/10.1038/lsa.2016.76

[22] X. Wan, M. Qi, T.Chen, and T.-J. Cui. "Field-programmable beam reconfiguring based on digitally-controlled coding metasurface," *Sci Rep* 6, 20663 (2016). https://doi.org/10.1038/srep20663

[23] J. Huang, C.-X. Wang, Y. Sun, *et al.*, "Reconfigurable intelligent surfaces: Channel characterization and modeling," *Proc. IEEE*, vol. 110, no. 9, pp. 1290–1311, Sept. 2022.

[24] M. Rahal, B. Denis, T. Mazloum, F. Munoz, and R. D'Errico, "RIS-aided positioning experiments based on mmWave indoor channel measurements," in Proc. *IPIN'23*, Nuremberg, Germany, 2023, pp. 1-6.

[25] Y. Li, Y. Wang, Y. Chen, Z. Yu, and C. Han, "Channel measurement and coverage analysis for NIRS-aided THz communications in indoor environments," *IEEE Commun. Lett.*, vol. 27, no. 9, pp. 2486-2490, Sept. 2023.

[26] X. Pei, H. Yin, L. Tan, L. Cao, Z. Li, K. Wang, K. Zhang, and E. Bjornson, "RIS-aided wireless communications: prototyping, adaptive beamforming, and indoor/outdoor field trials," *IEEE Trans. Commun.*, vol. 69, no. 12, pp. 8627-8640, Dec. 2021.

[27] Z. Wang, L. Tan, H. Yin, K. Wang, X. Pei and D. Gesbert,"A received power model for reconfigurable intelligent surface and measurement-based validations," in Proc. *SPAWC*, Lucca, Italy, 2021, pp. 561-565.

[28] W. Tang, X. Chen, M. Chen, *et al.*, "Path loss modeling and measurements for reconfigurable intelligent surfaces in the millimeter-Wave frequency band," *IEEE Trans. Commun.*, vol. 70, no. 9, pp. 6259–6276, Sept. 2022.

[29] R. Zhou, X. Chen, W. Tang, *et al.*, "Modeling and measurements for multi-path mitigation with reconfigurable intelligent surfaces," in *Proc. EuCAP'22*, Madrid, Spain, Mar. 2022, pp. 1–5.

[30] A. Mudonhi, M. Lotti, A. Clemente, R. D'Errico, and C. Oestges, "Impact of a transmitting-RIS on the geometrical structure of indoor mmWave channels," in *Proc. EuCAP'22*, Madrid, Spain, Mar. 2022, pp. 1–5.

[31] G. Li, L. Hu, P. Staat, *et al.*, "Reconfigurable intelligent surface for physical layer key generation: constructive or destructive?" *IEEE Wireless Commun.*, vol. 29, no. 4, pp. 146–153, Aug. 2022.

[32] W. Tang, M. Z. Chen, X. Chen, *et al.*, "Wireless communications with reconfigurable intelligent surface: Path loss modeling and experimental measurement," *IEEE Trans. Wireless Commun.*, vol. 20, no. 1, pp. 421–439, Jan. 2021.

[33] X. Cai, B. Peng, X. Yin, and A. P. Yuste, "Hough-transform-based cluster identification and modeling for V2V channels based on measurements," *IEEE Trans. Veh. Technol.*, vol. 67, no. 5, pp. 3838–3852, May 2018.

[34] J. Huang, C.-X. Wang, H. Chang, J. Sun, and X. Gao, "Multi-frequency multi-scenario millimeter wave MIMO channel measurements and modeling for B5G wireless communication systems," *IEEE J. Sel. Areas Commun.*, vol. 38, no. 9, pp. 2010–2025, Sept. 2020.

[35] B. H. Fleury, M. Tschudin, R. Heddergott, D. Dahlhaus, and K. I. Pedersen, "Channel parameter estimation in mobile radio environments using the SAGE algorithm," *IEEE J. Sel. Areas Commun.*, vol. 17, no. 3, pp. 434–450, Mar. 1999.

[36] J. Huang, C.-X. Wang, R. Feng, J. Sun, W. Zhang, and Y. Yang, "Multi frequency mmWave massive MIMO channel measurements and characterization for 5G wireless communication systems," *IEEE J. Sel. Areas Commun.*, vol. 35, no. 7, pp. 1591–1605, Jul. 2017.

[37] G. R. MacCartney, S. Deng, and T. S. Rappaport, "Indoor office plan environment and layout-based mmWave path loss models for 28 GHz and 73 GHz," in *Proc. VTC Spring'16*, Nanjing, China, May 2016, pp. 1–6.

[38] Z. Zhou, L. Zhang, X. Chen, C.-X. Wang, and J. Huang, "Multi-frequency wireless channel measurements and characteristics analysis in indoor corridor scenarios," in *Proc. VTC Fall'21*, Norman, OK, USA, Sept. 2021, pp. 1–5.

[39] E. Tsakalaki, O. N. Alrabadi, W. Fan, and G. F. Pedersen, "Covariance based spatial channel structure emulation for MIMO OTA testing," *IEEE Commun. Lett.*, vol. 18, no. 2, pp. 205–208, Feb. 2014.

[40] E. Telatar, "Capacity of multi-antenna gaussian channels," *Eur. Trans. Telecommun.*, vol. 10, no. 6, pp. 585–595, Nov. 1999.

[41] V. Jungnickel, S. Jaeckel, L. Thiele, *et al.*, "Capacity measurements in a cooperative MIMO network," *IEEE Trans. Veh. Technol.*, vol. 58, no. 5, pp. 2392–2405, June 2009.

[42] G. L. Foschini and M. J. Gans, "On limits of wireless communications in a fading environment when using multiple antennas," *Wireless Pers. Commun.*, vol. 6, no. 3, pp. 311–335, 1998.

[43] Y. Cui, P. Li, Z. Ye, Y. Wu, and J. Wu, "Research of reconfigurable intelligent surface deployment for wireless communication networks," *Radio Commun. Tech.,* vol. 48, no. 2, pp. 291–296, Jan. 2022.

Response to the Reviewers' Comments on VT-2023-04381: "RIS-Assisted MIMO Channel Measurements and Characteristics Analysis for 6G Wireless Communication Systems"

The authors would like to thank the editor and all of the reviewers for their helpful and insightful comments. We have improved the quality of the manuscript by carefully taking all the comments into account. The modifications in the revised manuscript as well as the response to the reviewers' comments are described below.

Associate Editor

Please avoid defining unnecessary acronyms in the abstract of the paper.

Response: According to the document "IEEE Editorial Style Manual" (https://www.ieee.org/content/dam/ieee-org/ieee/web/org/conferences/style_references_manual.pdf), we keep the acronyms in the abstract of the revised manuscript. The rule on Page 3 states that "***Define acronyms the first time they appear in the Abstract*** *as well as the first time they appear in the body of the paper, written out as part of the sentence, followed by the acronym in parentheses.*"

Reviewer 1

The article deals with a study of the characterization of a 5.4 GHz RIS in an anechoic room, indoor environment and outdoors. The article is well structured, written in a good English and the reviewer believes that it is a very interesting work.

1. Reviewer does not understand why the authors decided to submit it to IEEE Vehicular Technology, since there is not the slightest reference to vehicular communication. The reviewer suggests at least mentioning some applications that can be carried out in the field of vehicular communications with the RIS studied.

Response: In the revised manuscript, we have added 4 references ([10]-[13]) and the corresponding explanations related to the field of vehicular communications in the introduction on Page 1 as follows:

"*In the area of vehicular communications, RIS also plays an important role. In [10], RIS was used in vehicular communication systems to implement robust transmissions with statistical channel state information. In [11], a method of RIS selection in vehicular communication networks was introduced to realize a higher ergodic capacity. In [12], the authors jointly optimized RIS beamforming and vehicle trajectory to minimize the power consumption. In [13], a joint optimization problem considering both the vehicle power allocation and RIS* *beamforming was discussed to maximize the throughput.*"

References:
[10] Y. Chen, Y. Wang, and L. Jiao, "Robust transmission for reconfigurable intelligent surface aided millimeter wave vehicular communications with statistical CSI," *IEEE Trans. Wireless Commun.*, vol. 21, no. 2, pp. 928-944, Feb. 2022.
[11] N. Mensi, and D. B. Rawat, "Reconfigurable intelligent surface selection for wireless vehicular communications," *IEEE Wireless Commun. Lett.*, vol. 11, no. 8, pp. 1743-1747, Aug. 2022.
[12] A. B. M. Adam, X. Wan, M. A. M. Elhassan, *et al.*, "Intelligent and robust UAV-aided multiuser RIS communication technique with jittering UAV and imperfect hardware constraints," *IEEE Trans. Veh. Technol.*, vol. 72, no. 8, pp. 10737-10753, Aug. 2023.
[13] Y. Yu, X. Liu, Z. Liu, and T. S. Durrani, "Joint trajectory and resource optimization for RIS assisted UAV cognitive radio," *IEEE Trans. Veh. Technol.*, vol. 72, no. 10, pp. 13643-13648, Oct. 2023.

2. When the authors refer to coplane-nocoplane measurements the reviewer has difficulty understanding. From fig.4 it seems that the reference system changes in the two measurements, how is this possible? And it seems that the RIS has "its back" to the transmitter. The reviewer does not understand the meaning of these measures, so strongly believes that this part needs to be clarified and explained better. Perhaps it could also help by adding arrows to the figures, which explain the path that changes between the 2 configurations.

Response: In the revised manuscript, we have added Fig. 5 to illustrate the meanings of "coplane" and "non-coplane", and further clarified the difference. Coplane configuration means that the Tx, Rx, and normal line of RIS lie in the same plane. Non-coplane configuration means that they are not in the same plane. We can also denote the plane constituted by the Tx and the RIS normal line as $P_{Tx\text{-}Z}$ and the plane constituted by the Rx and the RIS normal line as $P_{Rx\text{-}Z}$. The coplane configuration means that $P_{Tx\text{-}Z}$ and $P_{Rx\text{-}Z}$ are in the same plane. The non-coplane configuration means that $P_{Tx\text{-}Z}$ and $P_{Rx\text{-}Z}$ are in different planes.

The following paragraph on page 4 has been added:

"*The illustration of these two configurations is shown in Fig. 5. The Tx and normal line of RIS can constitute a plane denoted as $P_{Tx\text{-}Z}$, while the Rx and normal line of RIS can constitute a plane denoted as $P_{Rx\text{-}Z}$. Coplane configuration means that $P_{Tx\text{-}Z}$ and $P_{Rx\text{-}Z}$ are the same plane. Non-coplane configuration means that $P_{Tx\text{-}Z}$ and $P_{Rx\text{-}Z}$ are different planes.*"

3. Report in the text the mathematical meaning of the insertion loss (10*log10(pint/pout)) or how it was calculated.

Response: In the revised manuscript, we have added the text to elaborate the meaning of insertion loss in the last paragraph on Page 6 as follows:

"*When calculating the insertion loss, the* S_{21} *value of the metal plate is used as a benchmark. The insertion values of RIS under different coding states are calculated as the differences between the* S_{21} *values of RIS and that of the metal plate.*"

4. In figure 8 above with the purple line and purple dots the authors refer to the results with the metal plate, while in the bottom one to an average value. It is necessary to either change the color/shape of the curve or specify that the curve at the bottom also refers to the metal plate (?).

Response: In the revised manuscript, we have changed the color of the curve "Mean value" from purple to green in Fig. 9(b) (Fig. 8(b) in the original manuscript).

5. Check all the English, page 11 of 13 subsection 4) : double "In in"

Response: In the revised manuscript, we have further improved the English writing to avoid any typos.

Reviewer 2

In this work, the authors present channel measurements and analysis for RIS-assisted MIMO systems. The topic is timely and interesting, and the motivation and novelty is well discussed. There are no major flaws in the paper and the reviewer has the following comments to improve the manuscript:

1. The abstract needs to be optimized a bit to highlight well also the motivation of this work.

Response: In the revised manuscript, we have further improved the quality of the abstract and highlighted the motivation of this work as follows:

"*However, there exists little research on RIS small-scale fading channel measurements, which are important for the characterization of RIS channels and communication system design.*"

2. In the first paragraph, there is an excessive usage of the word RIS. Please consider rewriting for example as:
a) Owing to the advantages of RIS, such as easy-----> Owing to the advantages such as easy....
b) RIS has been regarded as a promising key...-----> it has been regarded as a promising key

Response: In the revised manuscript, we have rewritten the first paragraph on Page 1 as suggested. The revised sentence is as follows:

"*Owing to the advantages such as easy to deploy, energy-efficient, and low-cost, it has been regarded as a promising key technology for the sixth generation (6G) wireless communications [5]-[7].*"

3. Page 3, column 1: Your line "When conducting the segmented channel measurements for RIS-UE sub-channel, Tx is set at RIS side and Rx is set at UE side" is not clear. When the RIS is treated as TX, does it need to have RF chains for signal transmission?

Response: Note that RIS is regarded as a kind of passive device in this paper. So, there are no RF chains for RIS. The objective of segmented channel measurements is obtaining the channel characteristics for the BS-RIS/RIS-UE sub-channels. The signal path in the original channel is BS-RIS-UE. When conducting BS-RIS sub-channel measurements, RIS is replaced by the Rx (with RF chains) and BS is replaced by the Tx (with RF chains). When conducting RIS-UE sub-channel measurements, RIS is replaced by the Tx (with RF chains) and UE is replaced by the Rx (with RF chains). The Tx/Rx here means the channel measurement equipment which can transmit/receive wireless signals. To make it clear, we have changed the explanation in the second paragraph on Page 2 in the revised manuscript as the following:

"*It should be noticed that the words "Tx" and "the receiver (Rx)" here mean the channel measurement equipment which can transmit/receive wireless signals with radio frequency (RF) chains. When conducting the segmented channel measurements for the BS-RIS sub-channel, the Tx is placed at the BS position and the Rx is placed at the position of RIS to measure the channel between the BS and RIS. When conducting the segmented channel measurements for the RIS-UE sub-channel, the Tx is set at the position of RIS and the Rx is set at the position of UE to measure the channel between the RIS and UE.*"

4. Your bullets claiming the novelty of this work must also mention the used SAGE algorithm and why do you do the data processing as a motivation. Otherwise, the reader reads all the bullets only regarding the main novelty of this work and then in the paper organization finds "Section III presents the measurement data processing methods employing the the high-resolution Space Alternating Generalized Expectation Maximization (SAGE) algorithm." which has not been mentioned anywhere before.

Response: In the revised manuscript, we have added the SAGE based data processing as one novelty of this work as suggested.

5. In the same line " data processing methods employing the the high-resolution Space Alternating Generalized Expectation " ---> remove one "the"

Response: In the revised manuscript, we have revised as suggested.

6. Same page, column 2: "There are two different coding modes, the far-field coding mode and the nearfield coding mode." Please consider elaborating on this by providing a few details (Maybe only in the Introduction section, so that it is clear to the readers what you mean)

Response: In the revised manuscript, we have elaborated the coding methods in the introduction as suggested (see the first paragraph at the right column on Page 2):

"*Far-field and near-field coding methods are designed for the experiments. Far-field coding only considers the phase differences caused by the projection differences of the incident wave on the array. Near-field coding considers the phase differences among RIS elements caused by the differences of the distance from each RIS element to Rx. The detailed calculation methods will be given later in Section II.*"

7. Page 4, Col. 1, line 35: "The discrete phase is the most close phase to the continuous one among the four phases corresponding four codes." This is not clear. Please consider rewriting it, maybe be mentioned in terms of quantization error.

Response: In the revised manuscript, we have added TABLE II on Page 3 to illustrate the relationship between continuous phases and the codes.

8. Page 8, Col. 1, line 49: What's more, the difference between the power of the main lobe and that of side.... "What's more" does not sound right in a scientific paper. Please consider rewriting the line.

Response: In the revised manuscript, we have changed the word "What's more" into a more scientific word "Furthermore" on Page 7.